NANO LETTERS

Letter

pubs.acs.org/NanoLett

Immobilizing Individual Atoms beneath a Corrugated Single Layer of Boron Nitride

Huanyao Cun,[†] Marcella Iannuzzi,[‡] Adrian Hemmi,[†] Silvan Roth,[†] Jürg Osterwalder,[†] and Thomas Greber*[,†]

[†]Physik-Institut and [‡]Physikalisch-Chemisches Institut, Universität Zürich, Winterthurerstrasse 190, CH-8057 Zürich, Switzerland

ABSTRACT: Single atoms, and in particular the least reactive noble gases, are difficult to immobilize at room temperature. Ion implantation into a crystal lattice has this capability, but the randomness of the involved processes does not permit much control over their distribution within the solid. Here we demonstrate that the boron nitride nanomesh, a corrugated single layer of hexagonal boron nitride (h-BN) with a 3.2 nm honeycomb superstructure formed on a Rh(111) surface, can trap individual argon atoms at distinct subsurface sites at room temperature. A kinetic energy window for implantation is identified where the argon ions can penetrate the h-BN layer but not enter the Rh lattice. Scanning tunneling microscopy and photoemission data show the presence of argon atoms at two distinct sites within the nanomesh unit cell, confirmed also by density functional theory calculations. The single atom implants are stable in air. Annealing of implanted structures to 900 K induces the formation of highly regular holes of 2 nm diameter in the h-BN layer with adjacent flakes of the same size found on top of the layer. We explain this "can-opener" effect by the presence of a vacancy defect, generated during the penetration of the Ar ion through the h-BN lattice, and propagating along the rim of a nanomesh pore where the h-BN lattice is highly bent. The reported effects are also observed in graphene on ruthenium and for neon atoms.

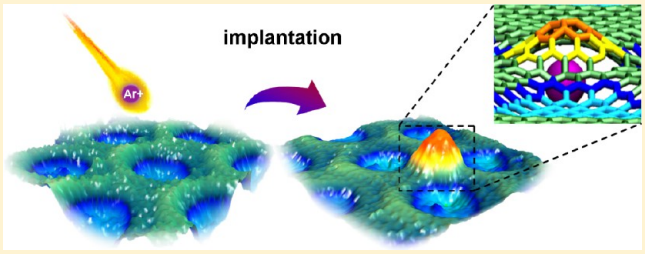

KEYWORDS: *Hexagonal boron nitride, graphene, single atom, implantation, defects, cutting single layers*

Modern nanotemplates based on hexagonal boron nitride or graphene[1] are robust and promising substrates for self-assembly,[2−5] electron confinement[6−8] or intercalation.[9−13] They exhibit superstructures with a lateral size of some nanometers, where the modulation of the registry within the large unit cell gives rise to new properties. Essentially, they consist in a single layer of sp^2 hybridized boron nitride or carbon that grows in a chemical vapor deposition or segregation process on substrates, where the lattice misfit between substrate and the sp^2 layer determines the super cell size.

If it comes to the implementation of such materials in macroscopic devices, it is a central issue to further control and structure them, ideally with fast methods such as ion irradiation. Irradiation with ions is known to lead to a variety of phenomena, for instance, formation of structures with quantum size effects,[14] site-selective etching,[15] or if highly charged ions are used, to hillock formation.[16] Here we report on site-selective placing of ions, which is a new form of single atom delta doping[17] with atomic precision. This finding may have a significant impact whenever single atoms shall be addressed, as it is, for example, the case in diamond NV centers[18] or single molecule magnets.[19] In the following, the term implantation is used for the process of penetration of low energy ions through the sp^2 layer and their stabilization as interstitial species, although the same term is commonly used for high energy ions.[20] The implantation induces vacancy defects, strain in the sp^2 layer, and enables further processes, which result in nonequilibrium structures. In particular, as a consequence of implantation, molecularly sharp, nanometer-sized flakes can be cut out of the sp^2 layers.

Defect-free monolayers of hexagonal boron nitride[21] and graphene[22] are expected to be impermeable for atoms and to act as perfect membranes. The strong σ-bonds with a strength in the order of 10 eV provide a robust network, which is rather inert to chemical attack. If atoms penetrate an sp^2 layer, they need significant energies that can lead to knocking out of constituent atoms. On the other hand, the implantation between the sp^2 layer and the substrate implies that the atoms do not penetrate deeper into the substrate, which imposes an upper bound to the ion energy. For the case of argon and rhodium, this upper threshold energy, where Ar may penetrate below the first Rh layer, is about 60 eV after BN penetration, as estimated from the Rh displacement energy[23] and the mass ratio between Ar and Rh. The predicted displacement energy for B or N is about 20 eV,[24] which opens an ion energy window for Ar implantation between the sp^2 layer and the substrate. Experimentally, the threshold energy for Ar penetration beneath the first layer of graphite was found to be 43.5 eV.[25] With post collision scanning tunneling microscopy and barrier height measurements, vacancy defects

Received: February 3, 2013
Revised: March 12, 2013
Published: April 3, 2013

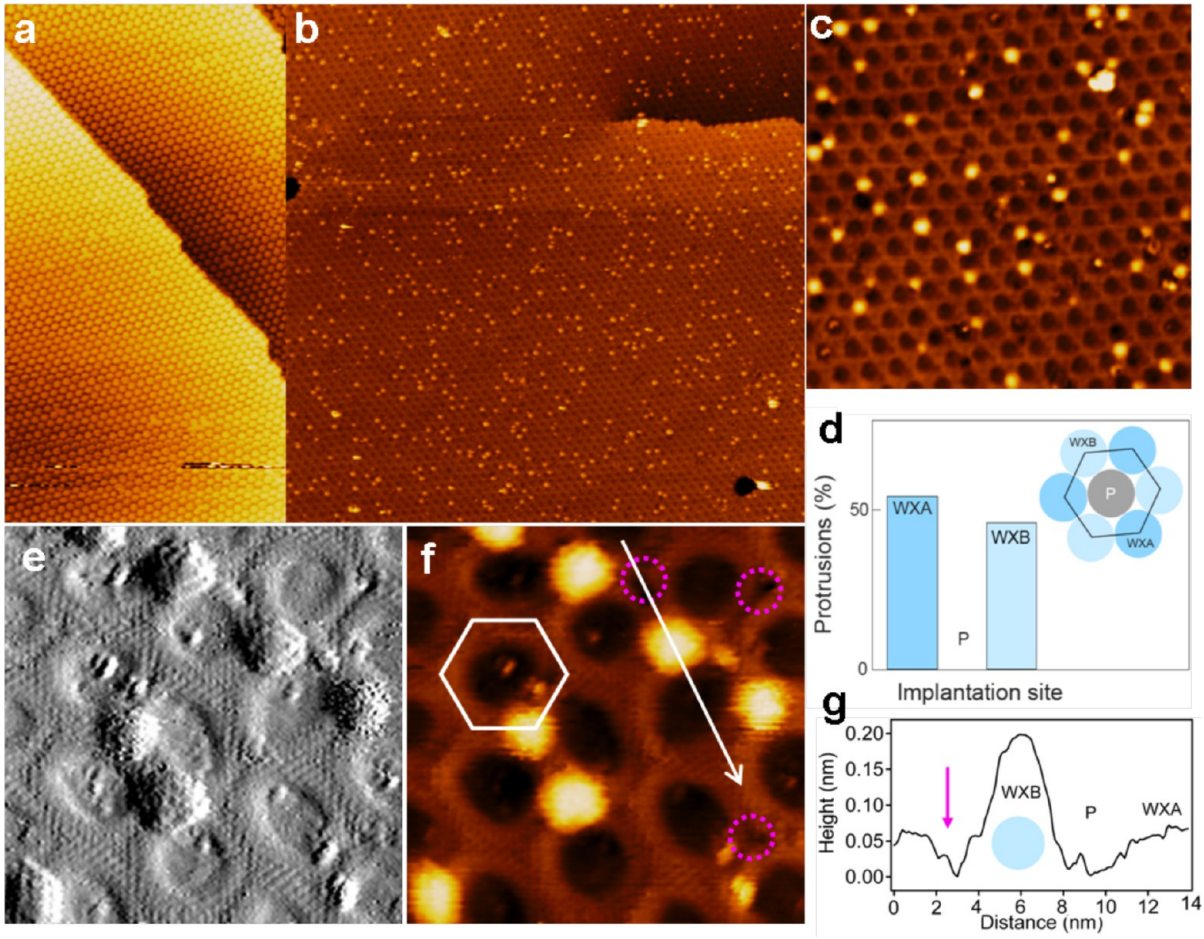

Figure 1. Room-temperature STM data of ion-implanted Ar below the h-BN/Rh(111) nanomesh. (a) Large-area image (104 × 190 nm^2) of clean h-BN/Rh(111), U_t = 1.00 V, I_t = 0.50 nA. (b) Large-scale image (190 × 190 nm^2) with Ar induced protrusions, U_t = −1.00 V, I_t = 0.50 nA. Without annealing the sputter charge density of about 250 nC/cm^2 produces 2 × 10^{12} protrusions/cm^2. (c) Zoom-in of panel b (45 × 45 nm^2) showing the selective placing of Ar in wires sites. (d) Statistics based on image panel b, which illustrates the selectivity of the process; Ar stops at two distinct sites beneath nanomesh wire crossings (WXA and WXB), but not in the pores (P). (e,f) Atomic-resolution STM current (e) and topography (f) images demonstrating Ar to be implanted beneath the h-BN wires. The bright protrusions are caused by interstitial Ar, and the pink circles indicate vacancy defects generated by the Ar penetration. The hexagon represents the honeycomb supercell, also shown in the inset of panel d; 11.4 × 11.4 nm^2, U_t = −1.10 V, I_t = 0.10 nA. (g) Cross section along the white line in panel f, the vacancy defect (arrow), an occupied WXB site, a pore and an empty WXA site are indicated.

due to the penetration and interstitial defects caused by the implanted atom at rest could be discriminated.[26] However, the interstitial site of the atoms could not be controlled. If an sp^2 target layer has different bonding sites to the substrate, it can be expected that superthermal atoms, which penetrate the sp^2 layer, thermalize at specific interstitial sites with a minimal strain energy.

The scenario of distinct sp^2 bonding sites is achieved with the h-BN nanomesh.[27] It is a single layer of hexagonal boron nitride on Rh(111), which forms a corrugated 12 × 12 superstructure with a lattice constant of 3.2 nm.[28] Because of the misfit between h-BN and Rh, and the preference of nitrogen to bond on top of Rh, the 13 × 13 BN units divide into bonding areas, the "pores" where the h-BN wets the substrate, and into "wires" where the h-BN has a pure van der Waals bonding to the substrate.

Figure 1 shows scanning tunneling microscopy data of the nanomesh before and after exposure to low energy Ar^+ ions corresponding to a sputter charge density of 1.6 × 10^{12} e/cm^2. The protrusions that emerge after ion exposure are situated at wire crossing sites WX and appear at a tunneling voltage of −1.1 V with a height of 0.175 ± 0.050 nm above the pore level. They have a robust signature and may be observed at positive and negative tunneling voltages. Hence, interstitial defects, where Ar atoms come to rest below the h-BN and above the Rh, are located where the nanomesh wires cross. The nanomesh honeycomb superstructure has two different wire crossing sites characterized by different registry to the substrate,[27,28] WXA and WXB. After ion exposure, the two sites are populated with distinct probabilities. Likely, the WXA/WXB branching ratio depends on ion beam parameters such as dose, energy, impact angle, and the annealing temperature. The selectivity of the implantation process is demonstrated in Figure 1d. For the large-scale image in Figure 1b, we count 0.2 protrusions per 12 × 12 Rh unit cell, where 54 ± 4% of the Ar atoms are trapped under WXA sites and no protrusions are found in the pores. The inset displays the hexagonal honeycomb super cell of h-BN/Rh(111) with the distinct regions that differ by the registry, that is, pore (P) and wire (W).

Figure 1e,f shows the corresponding current and topography STM images with atomic resolution. Intact h-BN clamps the Ar

dx.doi.org/10.1021/nl400449y | Nano Lett. 2013, 13, 2098−2103

such that it is fixed at room temperature. In the vicinity of the Ar protrusions, small defects are observed, which we assign to the vacancy defects after knock outs during Ar penetration. Figure 1g displays a line profile in Figure 1f that shows the height as measured from the bottom of the nanomesh pore. The cut runs across a defect generated by Ar implantation, a protrusion on a WXB site, and an area without defects (P) and in this case empty WXA site. If protrusions are formed, they also survive exposure to air.

The chemical identification of the implanted species was performed with X-ray photoelectron spectroscopy (XPS), as displayed in Figure 2a. The results were compared with STM

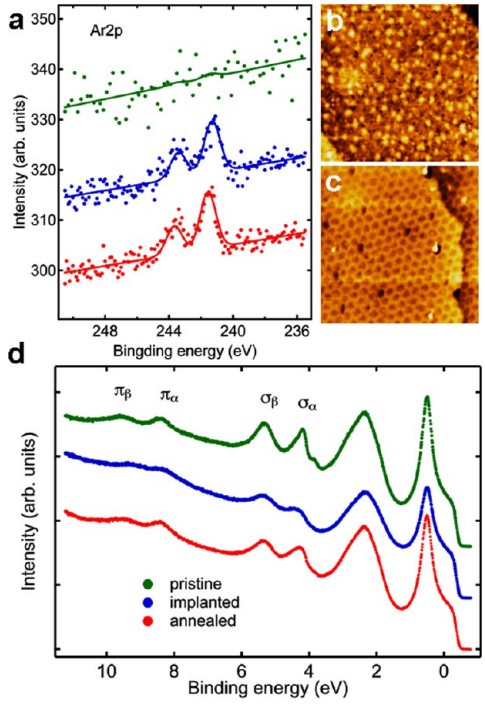

Figure 2. Photoemission spectra and corresponding STM images of h-BN/Ar/Rh(111) before and after annealing to 900 K. (a) Al Kα ($\hbar\omega$ = 1486.6 eV) XPS of Ar 2p core levels for pristine h-BN/Rh(111) (green, offset 30), Ar implanted (blue, offset 15), and after annealing (red). The Ar $2p_{3/2}$ binding energy of 241.3 eV shifts by 300 meV upon annealing, though the intensity is unaltered. (b,c) STM images of implanted h-BN/Ar/Rh(111) (sputter charge density 1050 nC/cm^2) before (b) and after (c) annealing. The bright protrusions in panel b are due to implanted Ar. After annealing, holes in the nanomesh pores and bright flakes can be observed (for details see Figure 4); (b) 50 × 50 nm^2, U_t = −1.00 V, I_t = 0.10 nA; (c) 50 × 50 nm^2, U_t = 1.00 V, I_t = 1.00 nA. (d) Normal emission UPS ($\hbar\omega$ = 21.2 eV) spectra of pristine h-BN/Rh(111) (green), Ar implanted (blue), and after annealing (red). The blue spectrum features a distinct broadening and intensity decrease of the σ_α, σ_β, π_α, and π_β bands. All peaks partially recover after annealing to 900 K.

images of the same preparation. The preparation shown in Figure 2b has a density of 0.9 protrusions per super cell. On the other hand, from the XPS atomic ratio of argon and boron, we determine a coverage of 2.3 Ar atoms per nanomesh super cell. This indicates that for this relatively large Ar dose the protrusions may host more than one Ar atom.

The STM image in Figure 2c, which was recorded after annealing to 900 K, shows that the protrusions disappear, meanwhile, holes at pore sites and some nearby bright flakes can be observed on the surface. We interpret these new structural features to be due to the "can-opener" effect that is described below. Intriguingly, XPS indicates no significant decrease of Ar in the interface, though a 0.3 eV core level binding energy increase, which rationalizes the disappearance of the interstitial defects upon ion implantation. Further search with STM for the Ar that remained in the interface showed blister-like objects that might house larger amounts of Ar. The above findings are as well confirmed by angular-resolved photoelectron spectroscopy (ARUPS), where the h-BN nanomesh has distinct signatures of the wire- and the pore-region.[27−29] Figure 2d shows the influence of the Ar implantation on the average valence band structure. The distinct BN bonding regions are reflected in the splitting of the σ-bands along the surface normal,[27−29] where the σ_α (σ_β) peaks at 4.2 (5.3) eV indicate hexagonal boron nitride on the wires (pores). Clearly, implantation of Ar distorts the σ_α bands, that is, the electronic structure in the wire regions and is thus consistent with the implantation of Ar at WX sites. The Ar dose is so small that it does not produce a significant Ar 3p level signature in the ARUPS spectra. If the implanted structure is annealed to 900 K, also the σ_β bands are affected: the σ_β intensity decreases with respect to the pristine mesh, while the σ_α intensity partially recovers.

Density functional theory (DFT) calculations based on the Gaussian and plane wave (GPW) formalism[30,31] were performed in order to rationalize the processes induced by Ar implantation. Different possible sites for the implantation have been tested by simply positioning an Ar atom between an intact h-BN layer and Rh and relaxing the structure. It has been found that beneath the pore the Ar atom is unstable and quickly moves toward the wire region. Beneath the wire, instead, the Ar atom can be stabilized at different sites. The differences in structure and energy are correlated with the registry of BN units with respect to the three high symmetry sites in the Rh(1 × 1) unit cell. In particular, wire sites with (B-top, N-hcp) registry are favored with respect to sites with (B-hcp, N-fcc) registry, which is consistent with the selectivity observed in the experiments. Hence, we call the former WXA and the latter WXB wire crossing sites. The presence of one Ar trapped beneath the wire induces the formation of a BN protrusion, whose peak is at 0.26 nm from the bottom of the pore. The up-lifted h-BN area involves about one-sixth of nanomesh unit cell. Figure 3a displays a three-dimensional view of a calculated structure of the h-BN nanomesh with implanted Ar. We also investigated the possibility of placing more Ar atoms together beneath the wire. A few Ar atoms placed in the same area tend to aggregate and form planar clusters. The larger the cluster, the higher and broader the protrusion gets. To date we succeeded to calculate structures with up to 6 Ar atoms per wire crossing.

Figure 3b shows four Tersoff−Hamann simulations[32] of the h-BN nanomesh, that is, the bare mesh, one Ar at the WXA site, one Ar at the WXB site, and two Ar atoms at the WXA site. The maximum height of the simulated STM topography is about 0.18 nm from the bottom of the pore in the case of one implanted Ar atom. It increases to more than 0.2 nm for two or more Ar atoms. The formation of the overlayer protrusion implies the distortion of h-BN with additional strain in the B−N bonds and the loss in attractive interaction energy between BN and Rh. Figure 3c displays the strain-distribution of the 507 B−N bonds in the super cell versus nitrogen atom height for the four structures in Figure 3b. Strain 0 corresponds to the calculated equilibrium B−N distance. Nitrogen atoms with a height above Rh between 0.2 and 0.25 nm belong to the pore.

dx.doi.org/10.1021/nl400449y | Nano Lett. 2013, 13, 2098−2103

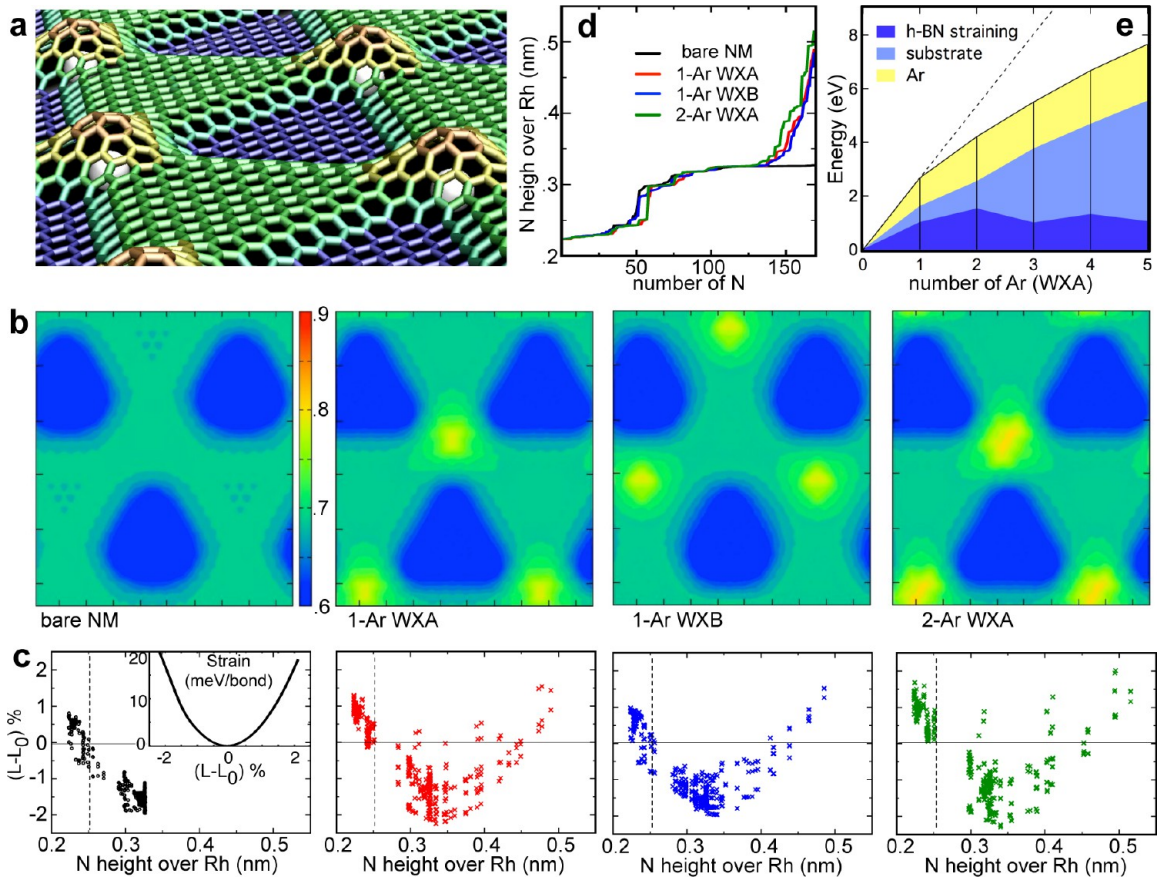

Figure 3. Density functional theory results on Ar implantation beneath the h-BN nanomesh. (a) Three dimensional view of the h-BN/Ar/Rh(111) structure with one Ar atom at a WXA wire crossing site. (b) Tersoff–Hamann simulations for four different structures, the bare nanomesh (NM), one Ar at WXA, one Ar at WXB, and two Ar atoms at WXA. The STM topography has been obtained with a bias potential of −1 eV and for a density of 10^{-4} e/nm^3. The color scale indicates the height above the topmost Rh layer in nm. (c) Strain of the B–N bonds given in percentual difference with respect to the calculated equilibrium bond length L_0, $(L-L_0)$%, versus the height of N atoms above Rh. The four panels correspond to the four structures in panel b. The inset in the first panel reports the energy increase in meV per bond as calculated by uniformly changing the bond length of a flat, freestanding h-BN layer. (d) Sorted height of the 169 nitrogen atoms of the NM unit cell. Interstitial Ar lifts about 30 nitrogen atoms. (e) Implantation energy versus number of Ar atoms in the WXA site. The energy cost per Ar atom decreases by increasing the cluster size, which predicts Ar clustering.

For the bare nanomesh, some bonds in the pore are slightly elongated to maximize the contact of N with Rh atoms. In order to match the 12 × 12 Rh units, the B–N bonds of the wire are typically contracted. After Ar implantation, many bonds of the up-lifted area turn out to be longer than in the bare nanomesh. However, the straining propagates also to bonds at the rim and in the pore.

Figure 3d shows the nitrogen atom height versus atom numbers for the four structures in Figure 3c. It can be seen that more than 30 nitrogen atoms are lifted up by the implantation. The uplift imposes a global work function shift of 80 meV. This work function increase is in agreement with experiments in Figure 2, where an extrapolated shift of 75 meV for one protrusion per supercell is found.

The total energy differences (implantation energies) with respect to a pristine nanomesh and an Ar atom in the vacuum are +2.6 eV (+3.7 eV) for WXA(WXB). Both structures are metastable and have a local minimum of strain in the substrate and the sp^2 layer. Figure 3e displays the WXA implantation energy for clusters of 1–5 Ar atoms. The total amount consists in compression energy of the Ar, strain-energy of the h-BN overlayer, strain energy of the substrate and loss in interaction energy between h-BN and substrate. It can be seen that the energy stored in the Ar atoms is about 30% of the implantation energy. The strain energy of the h-BN, which is the energy difference of the BN layer before and after the implantation, is in the same order of magnitude. Although the implantation energies are substantial and call for a hyperthermal process, they are still smaller than the displacement energy for B and N.[24] The first implant has to pay most energy, which is related to its wedge function. This provides a natural explanation for Ar clustering, mainly on WXA sites, if the temperature allows Ar diffusion beneath the wires.

Annealing of the implanted structures to 900 K leads to a peculiar response of the system: the cut-out of h-BN flakes from the nanomesh pores. Figure 4 shows a h-BN nanomesh sample exposed to a sputter charge density of 350 nC/cm^2 after annealing to 900 K. No Ar-related protrusions are visible anymore, though 2% of the 2 nm pores map dark, and some bright flakes are visible. In Figure 4a, the flakes display in a streaky fashion, which is due to dragging of these species by the STM tip. The zoom-in image in Figure 4b shows that the flakes lie close to dark pores with matching size. This allows the conjecture that the flakes correspond to h-BN cut-outs from the pores (see Figure 4c). The cutting temperature is well below the h-BN/Rh(111) disintegration at 1160 K.[33] Accordingly, no

dx.doi.org/10.1021/nl400449y | Nano Lett. 2013, 13, 2098–2103

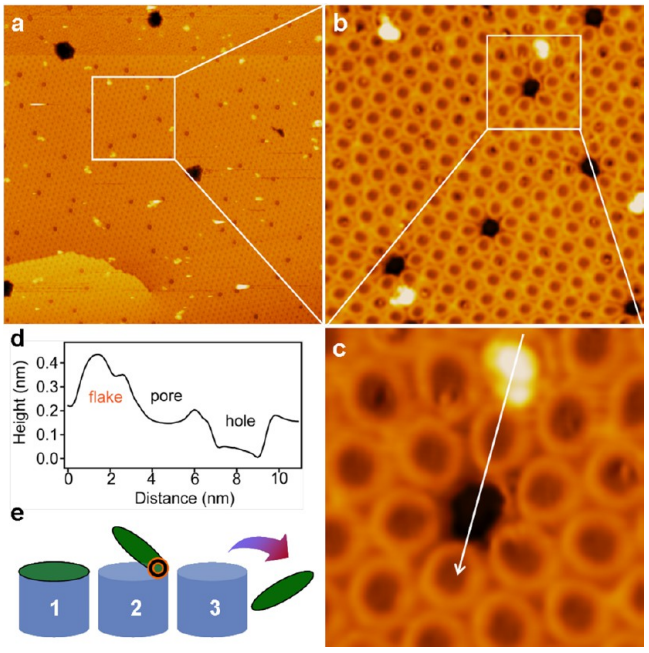

Figure 4. h-BN nanomesh after annealing of h-BN/Ar/Rh(111) to 900 K (sputter charge density 350 nC/cm^2). (a) Large-scale STM image (180 × 180 nm^2) showing 2 nm holes at pore sites. The bright flakes correspond to the 2 nm cut-outs. The large dark regions are defects of nanomesh existing prior to ion implantation, U_t = −1.10 V, I_t = 0.50 nA. (b) Zoom-in (46 × 46 nm^2) of the white frame in panel a with holes and corresponding flakes. (c) High-resolution image showing a hole and a flake, 14 × 14 nm^2, U_t = −1.10 V, I_t = 0.50 nA. (d) Cross-sectional profile along the white line in panel c, illustrating the size of the flake to be larger than the Ar clusters. It also shows the height difference between the flake and the holes. (e) Sketch of the can-opener effect. The green pieces represent the "cap", that is, the h-BN in the pore. The red-black circle is an active defect that promotes the cutting of the flake at the rim of the pore. The numbers 1, 2, and 3 indicate the sequence of the process.

such effect is observed, when samples without ion exposure are annealed to this temperature. Therefore ion exposure must create an active species that enables cutting (red-black circle in Figure 4e). Likely the defects due to the Ar implantation provoke the cutting of h-BN flakes out of the h-BN layer. For the following reasons we propose this "can-opener" effect to be related to the migration of the vacancy defects[34] to the nanomesh rim sites and the straining of the monatomic membrane upon implantation of Ar atoms. The can-opener mechanism breaks about 24 B−N bonds at the rim of the nanomesh pores (step 2 in Figure 4e). The cut pieces are not anymore bound to the h-BN network, and the relatively weak bonding to the Rh substrate, which is documented by the streaky imaging, may break. At 900 K, the cut h-BN flakes from the pores lift off and diffuse away from the original site (step 3 in Figure 4e). Taking the calculated B−N bond energy in borazine, the cutting costs 6.3 eV per bond.[35] If hydrogen assists the cutting effect, that is, if a dangling bond pair is saturated with hydrogen, the energy cost of 6.3 eV reduces to 0.8 eV, which can be provided by thermal fluctuations at 900 K, the implantation energy and/or a vacancy defect. Single interstitial Ar atoms produce strain up to 2% (see Figure 3d), hence not sufficient for the rupture of the h-BN, which was found to occur for strain beyond 4% in boron nitride nanotubes.[36] The high selectivity of the cut must be related to the fact that defect creation in sp^2 layers is more facile if the sheets are bent, as it was found for carbon nanotubes.[37]

Control experiments with neon ions also show site-selective implantation at nanomesh wire crossings and the can-opener mechanism. For the sister compound graphene on Ru(0001),[38−40] where the supercell contains as well strongly bound and a loosely bound regions,[41] we also observe implantation and the can-opener effect.

In conclusion, the controlled placing of single atoms on specific sites of a 3 nm honeycomb nanostructure consisting in one layer of boron nitride on a Rh substrate is reported. At room temperature, these atoms do not diffuse and remain protected by an ultimately thin membrane. Furthermore, the implantation process promotes the can-opener effect, that is, cutting-out of h-BN flakes with a diameter of 2 nm. This is a way to functionalize sp^2 layer templates, that is, to produce anchoring sites for suitable molecular precursors and allows the immobilization and use of single atoms at room temperature. The reported effects are robust and quite general: they also apply for graphene structures.

Methods. *Experimental Section.* The experiments were performed in two ultrahigh-vacuum (UHV) systems with base pressure of 1 × 10^{-10} mbar. One is a variable-temperature scanning tunneling microscope (Omicron VT-STM), and the other has a room-temperature STM (Park Scientific) combined with photoemission on the same sample.[9,42] The STM measurements were carried out with electrochemically etched tungsten tips. All STM images were taken in constant-current mode at room temperature. The h-BN nanomesh samples were produced with the standard recipe,[27] though the samples for the photoemission experiments were cleaned with Ne$^+$ ion sputtering. The ion implantation was achieved with a Specs IQP 10/35 Penning type ion sources run at lowest acceleration potential. The sputter charge density corresponds to the integrated sputter current density.

Theory. Calculations are performed using Kohn−Sham DFT within the GPW formalism as implemented in the Quickstep module in the CP2K program package.[43] Dual-space pseudopotentials[44] are used to describe the interaction of valence electrons with atomic cores. The pseudopotentials for boron and nitrogen assume 3 and 5 valence electrons, respectively. The atomic cores of the Rh are described by potentials with 9 valence electrons. The Gaussian basis sets chosen for this type of application are of the molecularly optimized type.[45] The PW energy cutoff for the expansion of the density is set at 500 Ry. The Brillouin zone is sampled only at the Γ-point. Exchange and correlation are calculated with the revised Perdew−Burke−Ernzerhof[46] GGA exchange-correlation functional. The latter is used together with the corrections for the dispersion interactions. Long-range dispersion interactions have been computed using DFT-D3 formalisms.[47] We employ a slablike model where the simulation cell consists of four layer of 12 × 12 Rh(111) units terminated on one side by a 13 × 13 h-BN over layer. Periodic boundary conditions are applied and interactions with periodic images in the direction perpendicular to the exposed surface are avoided by adding about 20 Å of vacuum space above the slab. The atoms of bottom Rh layer are kept fixed in the bulk positions. This computational setup has been already successfully applied for several previous studies related to h-BN/Rh(111).[13,48]

dx.doi.org/10.1021/nl400449y | *Nano Lett.* 2013, 13, 2098−2103

AUTHOR INFORMATION

Corresponding Author

*E-mail: greber@physik.uzh.ch. Phone: +41 (0)44 6355744. Fax: +41 (0)44 6355704.

Notes

The authors declare no competing financial interest.

ACKNOWLEDGMENTS

Financial support by the Swiss National Science Foundation is gratefully acknowledged. The Swiss National Supercomputer Centre (CSCS) is acknowledged for the generous allocation of computer time.

REFERENCES

(1) Goriachko, A.; Over, H. *Int. J. Res. Phys. Chem. Chem. Phys.* **2009**, *223*, 157−168.
(2) N'Diaye, A. T.; Bleikamp, S.; Feibelman, P. J.; Michely, T. *Phys. Rev. Lett.* **2006**, *97*, 215501.
(3) Dil, H.; Lobo-Checa, J.; Laskowski, R.; Blaha, P.; Berner, S.; Osterwalder, J.; Greber, T. *Science* **2008**, *319*, 1824−1826.
(4) Mao, J. H.; Zhang, H. G.; Jiang, Y. H.; Pan, Y.; Gao, M.; Xiao, W. D.; Gao, H. J. *J. Am. Chem. Soc.* **2009**, *131*, 14136.
(5) Pollard, A. J.; et al. *Angew. Chem. Int. Ed.* **2010**, *49*, 1794−1799.
(6) Zhang, H. G.; Hu, H.; Pan, Y.; Mao, J. H.; Gao, M.; Guo, H. M.; Du, S. X.; Greber, T.; Gao, H.-J. *J. Phys.: Condens. Matter.* **2010**, *22*, 302001.
(7) Borca, B.; Barja, S.; Garnica, M.; Sanchez-Portal, D.; Silkin, V. M.; Chulkov, E. V.; Hermanns, C. F.; Hinarejos, J. J.; Vazquez de Parga, A. L.; Arnau, A.; Echenique, P. M.; Miranda, R. *Phys. Rev. Lett.* **2010**, *105*, 036804.
(8) Subramaniam, D.; Libisch, F.; Li, Y.; Pauly, C.; Geringer, V.; Reiter, R.; Mashoff, T.; Liebmann, M.; Burgdörfer, J.; Busse, C.; Michely, T.; Mazzarello, R.; Pratzer, M.; Morgenstern, M. *Phys. Rev. Lett.* **2012**, *108*, 046801.
(9) Auwarter, W.; Muntwiler, M.; Greber, T.; Osterwalder, J. *Surf. Sci.* **2002**, *511*, 379−386.
(10) Sutter, P. W.; Flege, J.-I.; Sutter, E. A. *Nat. Mater.* **2008**, *7*, 406−411.
(11) Preobrajenski, A. B.; Ng, M. L.; Vinogradov, N. A.; Vinogradov, A. S.; Lundgren, E.; Mikkelsen, A.; Martensson, N. *Nano Lett.* **2009**, *9*, 2780−2787.
(12) Riedl, C.; Coletti, C.; Iwasaki, T.; Zakharov, A. A.; Starke, U. *Phys. Rev. Lett.* **2009**, *103*, 246804.
(13) Brugger, T.; Ma, H.; Iannuzzi, M.; Berner, S.; Winkler, A.; Hutter, J.; Osterwalder, J.; Greber, T. *Angew. Chem. Int. Ed.* **2010**, *49*, 6120−6124.
(14) Schmid, M.; Hebenstreit, W.; Varga, P.; Crampin, S. *Phys. Rev. Lett.* **1996**, *76*, 2298−2301.
(15) Broekmann, P.; Mewe, A.; Wormeester, H.; Poelsema, B. *Phys. Rev. Lett.* **2002**, *89*, 146102.
(16) Aumayr, F.; Facsko, S.; El-Said, A. S.; Trautmann, C.; Schleberger, M. *J. Phys.: Condens. Matter* **2011**, *23*, 393001.
(17) Harris, J. *J. Mater. Sci.- Mater. Electron* **1993**, *4*, 93−105.
(18) Gruber, A.; Drabenstedt, A.; Tietz, C.; Fleury, L.; Wrachtrup, J.; vonBorczyskowski, C. *Science* **1997**, *276*, 2012−2014.
(19) Ishikawa, N.; Sugita, M.; Ishikawa, T.; Koshihara, S.; Kaizu, Y. *J. Am. Chem. Soc.* **2003**, *125*, 8694−8695.
(20) Jain, I. P.; Agarwal, G. *Surf. Sci. Rep.* **2011**, *66*, 77−172.
(21) Sainsbury, T.; Satti, A.; May, P.; Wang, Z.; McGovern, I.; Gun'ko, Y. K.; Coleman, J. *J. Am. Chem. Soc.* **2012**, *134*, 18758−18771.
(22) Bunch, J. S.; Verbridge, S. S.; Alden, J. S.; van der Zande, A. M.; Parpia, J. M.; Craighead, H. G.; McEuen, P. L. *Nano Lett.* **2008**, *8*, 2458−2462.
(23) Kosugi, S.; Ishikawa, N.; Saitoh, Y.; Hori, F.; Iwase, A. *J. Nucl. Mater.* **2011**, *411*, 171−173.
(24) Kotakoski, J.; Jin, C. H.; Lehtinen, O.; Suenaga, K.; Krasheninnikov, A. V. *Phys. Rev. B* **2010**, *82*, 113404.
(25) Marton, D.; Boyd, K.; Lytle, T.; Rabalais, J. *Phys. Rev. B* **1993**, *48*, 6757−6766.
(26) Hahn, J.; Kang, H. *Phys. Rev. B* **1999**, *60*, 6007−6017.
(27) Corso, M.; Auwärter, W.; Muntwiler, M.; Tamai, A.; Greber, T.; Osterwalder, J. *Science* **2004**, *303*, 217−220.
(28) Berner, S.; Corso, M.; Widmer, R.; Groening, O.; Laskowski, R.; Blaha, P.; Schwarz, K.; Goriachko, A.; Over, H.; Gsell, S.; Schreck, M.; Sachdev, H.; Greber, T.; Osterwalder, J. *Angew. Chem. Int. Ed.* **2007**, *46*, 5115−5119.
(29) Goriachko, A.; He, Y.; Knapp, M.; Over, H.; Corso, M.; Brugger, T.; Berner, S.; Osterwalder, J.; Greber, T. *Langmuir* **2007**, *23*, 2928−2931.
(30) Lippert, G.; Hutter, J.; Parrinello, M. *Mol. Phys.* **1997**, *92*, 477−487.
(31) VandeVondele, J.; Krack, M.; Mohamed, F.; Parrinello, M.; Chassaing, T.; Hutter, J. *Comput. Phys. Commun.* **2005**, *167*, 103−128.
(32) Tersoff, J.; Hamann, D. *Phys. Rev. B* **1985**, *31*, 805−813.
(33) Dong, G.; Fourre, E. B.; Tabak, F. C.; Frenken, J. W. M. *Phys. Rev. Lett.* **2010**, *104*, 096102.
(34) Zobelli, A.; Ewels, C. P.; Gloter, A.; Seifert, G. *Phys. Rev. B* **2007**, *75*, 245402.
(35) Auwarter, W.; Suter, H.; Sachdev, H.; Greber, T. *Chem. Mater.* **2004**, *16*, 343−345.
(36) Wei, X.; Wang, M.-S.; Bando, Y.; Golberg, D. *Adv. Mater.* **2010**, *22*, 4895.
(37) Lu, A.; Pan, B. *Phys. Rev. Lett.* **2004**, *92*, 105504.
(38) Marchini, S.; Guenther, S.; Wintterlin, J. *Phys. Rev. B* **2007**, *76*, 075429.
(39) Vazquez de Parga, A. L.; Calleja, F.; Borca, B.; Passeggi, M. C. G., Jr.; Hinarejos, J. J.; Guinea, F.; Miranda, R. *Phys. Rev. Lett.* **2008**, *100*, 056807.
(40) Pan, Y.; Zhang, H.; Shi, D.; Sun, J.; Du, S.; Liu, F.; Gao, H.-J. *Adv. Mater.* **2009**, *21*, 2777.
(41) Brugger, T.; Guenther, S.; Wang, B.; Dil, J. H.; Bocquet, M.-L.; Osterwalder, J.; Wintterlin, J.; Greber, T. *Phys. Rev. B* **2009**, *79*, 045407.
(42) Greber, T.; Raetzo, O.; Kreutz, T.; Schwaller, P.; Deichmann, W.; Wetli, E.; Osterwalder, J. *Rev. Sci. Instrum.* **1997**, *68*, 4549−4554.
(43) CP2k developers group under the terms of the GNU General Public Licence; see http://www.cp2k.org. 2012.
(44) Goedecker, S.; Teter, M.; Hutter, J. *Phys. Rev. B* **1996**, *54*, 1703−1710.
(45) VandeVondele, J.; Hutter, J. *J. Chem. Phys.* **2007**, *127*, 114105.
(46) Zhang, Y.; Yang, W. *Phys. Rev. Lett.* **1998**, *80*, 890−891.
(47) Grimme, S.; Antony, J.; Ehrlich, S.; Krieg, H. *J. Chem. Phys.* **2010**, *132*, 154104.
(48) Ding, Y.; Iannuzzi, M.; Hutter, J. *J. Phys. Chem. C* **2011**, *115*, 13685−13692.